Geophysical Research Letters

RESEARCH LETTER
10.1029/2018GL079536

Key Points:
- We convert 1,202 horizontal seasonal GPS displacements into a strain field for California and surroundings
- Seasonal variations in dilatational strain vary regionally and, at least in northern California, are related to vertical displacements
- Seasonal strain may facilitate mainshock occurrence and causes an increase in earthquake magnitude and decrease in aftershock production

Supporting Information:
- Supporting Information S1
- Table S1
- Table S2
- Table S3
- Data Set S1
- Movie S1
- Movie S2
- Movie S3

Correspondence to:
C. Kreemer,
kreemer@unr.edu

Citation:
Kreemer, C., & Zaliapin, I. (2018). Spatiotemporal correlation between seasonal variations in seismicity and horizontal dilatational strain in California. *Geophysical Research Letters*, *45*. https://doi.org/10.1029/2018GL079536

Received 8 JUL 2018
Accepted 28 AUG 2018
Accepted article online 4 SEP 2018

Spatiotemporal Correlation Between Seasonal Variations in Seismicity and Horizontal Dilatational Strain in California

Corné Kreemer[1,2] **and Ilya Zaliapin**[3]

[1]Nevada Bureau of Mines and Geology, University of Nevada, Reno, Reno, NV, USA, [2]Nevada Seismological Laboratory, University of Nevada, Reno, Reno, NV, USA, [3]Department of Mathematics and Statistics, University of Nevada, Reno, Reno, NV, USA

Abstract We extract significant spatially coherent strain variations from horizontal seasonal Global Positioning System (GPS) displacements in the American Southwest. The dilatational strain is largest in northern California with maximum margin-normal contraction and extension in spring and fall, respectively, consistent with the Earth's surface going down and up at those times. The northern California signal has a phase shift with respect to that in southern California and the Great Basin. For northern and southern California the proportion of larger earthquakes are in-phase and the aftershock productivity out of phase with the inferred Coulomb stress on the San Andreas fault system. The intensity of mainshocks is in-phase in the north as well but not in the south. This suggests that a seasonal increase in fault-normal extension may or may not trigger mainshocks, but when an earthquake happens at those times, they grow larger than they otherwise would, which would cause a larger stress reduction and result in fewer aftershocks.

Plain Language Summary The changing amount of water and snow mass that lays on top of the Earth's surface is one possible explanation for observed seasonal variations in seismicity. This hydrological loading would change the state of stress inside the crust minutely with the seasons. We image the seasonal stress variation by using the horizontal seasonal displacements of GPS monuments in the southwestern United States. This reveals large-scale seasonal patterns of the crust contracting and extending in-phase with the Earth's surface going down and up, respectively, particularly in northern California which experiences a large excess of water and snow in late winter. The seasonal variations in horizontal deformation there correspond to variations in the number of mainshocks, with more earthquakes occurring when the crust is under extension. In southern California, we see no correlation with the number of mainshocks. In both regions, seasonal deformation correlates with the proportion of large earthquakes and shows an anticorrelation with the aftershock production. So even though seasonal deformation may not directly trigger earthquakes, if an earthquake happens during the right season, it seems to be able to grow a little larger, releasing a little more stress than it otherwise would and reducing the need for (more) aftershocks.

1. Introduction

The relationship between slip on a fault (i.e., an earthquake) and the accumulation or change in stress onto the fault is central to understanding seismogenesis. Observed seasonal variations in the number of earthquakes (i.e., *seismic intensity*) (Ader & Avouac, 2013; Bollinger et al., 2007; Christiansen et al., 2007; Craig et al., 2017; Dutilleul et al., 2015; Gao et al., 2000; Matsumura, 1986; Panza et al., 2011) provide means to assess the type and magnitude of stress perturbations, as well as a fault's frictional properties, required to advance or retard the buildup of stress on faults toward earthquake nucleation (Ader et al., 2014). Mechanisms that could provide seasonal stress perturbations fall into two categories: those intrinsic to the rock (e.g., temperature) or extrinsic (e.g., loading of the atmosphere, hydrosphere, or cryosphere onto Earth's surface). Most correlation studies have focused on the link between seismic intensity and snow/hydrologic loading (Amos et al., 2014; Bettinelli et al., 2008; Bollinger et al., 2007; Braunmiller et al., 2014; Craig et al., 2017; Heki, 2003; Pollitz et al., 2013).

Annual variations in the above-mentioned mechanisms are predicted and can also be seen in the solid Earth's deformation response captured by geodetic measurements. For example, seasonal displacements in GPS time series have been correlated with annual variations in atmospheric pressure (e.g., van Dam et al.,

1994), surface temperature (Prawirodirdjo et al., 2006), snow (Drouin et al., 2016; Heki, 2001) or water loading (Bettinelli et al., 2008; van Dam et al., 2001), or a combination therein (Johnson et al., 2017b; Tsai, 2011). The majority of the above studies used vertical GPS displacement time series, but the effect of surface loading has also been seen in horizontal time series (Argus et al., 2005; Chanard et al., 2014; Elósegui et al., 2003; Fu et al., 2013; Grapenthin et al., 2006; Kraner et al., 2018).

In previous studies the connection between seasonality in GPS time series and in seismic intensity was made through a physical model that would explain the geodetic data while providing a seasonal forcing mechanism (Amos et al., 2014; Bettinelli et al., 2008; Craig et al., 2017; Johnson et al., 2017a, 2017b). Furthermore, those studies only used the vertical GPS displacements. Here we convert horizontal seasonal displacements of GPS stations into the corresponding horizontal spatiotemporal variation in geodetic strain. These strains provide a more direct observable to compare with seismicity than modeled stress. Moreover, we apply this to the greater California area where the majority of the faults dip steeply and horizontal seasonal strain variations are expected to reflect stress perturbations on a fault in a more straightforward manner than vertical displacement variations would. We report strong spatiotemporal correlations between mainshock intensity, aftershock production, and the proportion of large events and the dilatational component of the horizontal seasonal geodetic strain field.

2. Seasonal Geodetic Displacements and Strain

We consider time series between 2002.00 and 2018.25 from all continuous GPS stations in our study area (i.e., the area shown in Figure 1 plus an additional 1° on each side). Time series are obtained from the Nevada Geodetic Laboratory (Blewitt et al., 2018). We exclude those stations for which the time series are $<$2.5 year long, those within California's Great Valley where stations' seasonal signal is significantly different from those on adjacent bedrock (Amos et al., 2014), and those with significant transient signals not associated with known earthquakes. For those stations affected by a large nearby earthquake we exclude the part of the post-seismic time series that exhibits transient motion. We analyze time series of the remaining 1,202 stations in the NA12 reference frame (Blewitt et al., 2013), which has removed daily continental-scale common mode displacements present in the IGS08 frame, including periodic loading signals related to hemisphere-scale water transport (Blewitt et al., 2001; Wu et al., 2003). Our analysis in NA12 therefore differs slightly with that in IGS08, because (1) the common mode signal is not exclusively periodic causing some slight differences in the estimation of the seasonal signal and (2) the continental-scale water loading cycle causes a small N-S oriented displacement gradient across our study area that yields a uniform strain of up to $\sim \pm 0.5 \times 10^{-9}$ in fall and spring, respectively. Both aspects combined affect our analysis only in a very minor way.

To each station's north, east, and vertical daily position time series, we fit a model that includes a rate, periodic signal, and offsets due to equipment changes and earthquake coseismic offsets. The periodic signal consists of an annual term and a semiannual term. We assume that the seasonal signal is constant over the period considered, which is generally an appropriate approximation. For clarity we present (horizontal) data and strain models that exclude 419 outlier stations but show in the supporting information nearly identical results for strain models based on all data. The outlier removal is explained in the supporting information as well.

Figure 1a shows the maximum horizontal vector displacement and its phase within the first half of the year. For simplicity we only show the values associated with the annual term, which has an amplitude that is on average 3.3 times larger than for the semiannual term. For comparison, we also show the vertical seasonal displacement (Figure 1b).

As evident from Figure 1a and especially Figure S1 (which includes outlier stations), the horizontal seasonal displacements (i.e., those predicted from the periodic signal we fit) are scattered, much more so than the vertical seasonal displacements. Nevertheless, some patterns are evident. Most coastal stations exhibit a maximum displacement toward the North American continent in March. This signal is most coherent in northern California. Stations east of the northern Sierra Nevada Mountains, in western Nevada, show oceanward motion that peaks in April. These signals are likely linked to the widespread subsidence of most of northern California that peaks in April (Figure 1b). Where vertical displacements are negligible (e.g., Great Basin and Mojave Desert), horizontal displacements seemingly show little spatial coherency. However, it is noteworthy that the maximum horizontal and vertical displacements in the Mojave Desert and

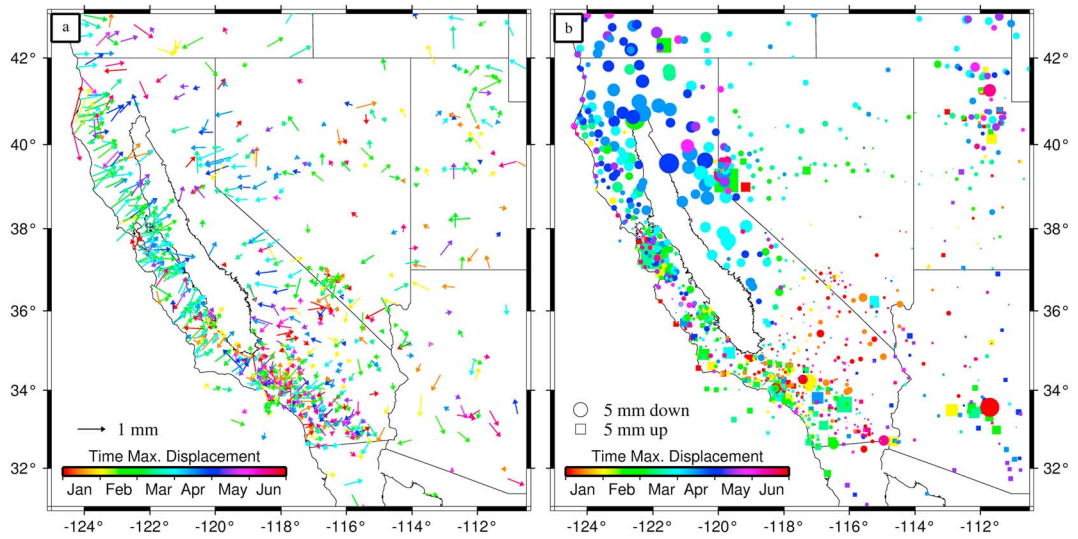

Figure 1. (a) Magnitude and azimuth of maximum horizontal displacement of annual periodicity (obtained from model fit to GPS time series) in the first half of the year. Colors indicate when in those 6 months the maximum displacement is reached. Outlier stations are omitted (Figure S1 shows all displacements). Black outline is for California's Great Valley, within which stations are excluded. (b) Size of circles is maximum vertical displacement of annual periodicity. Colors indicate the same as in Figure 1a, and circles and squares indicate whether the maximum displacement is down or up, respectively, in first half of the year.

southernmost California occur in early summer, distinctly later than in northern California. Finally, while the peak vertical displacement in the first 6 months is down in most of the study area, it is consistently up in Arizona and in the coastal areas of southern California.

Because of the noise in the displacements, regionally coherent seasonal strain signals may not be obvious from a visual inspection of the displacements. To extract such strain signal, we use the MELD (Median Estimation of Local Deformation) algorithm of Kreemer et al. (2018), which is robust against outlier data and is particularly well suited to retrieve long-wavelength signals. MELD does not consider the uncertainty in the input data and merely extracts a robust strain signal from many noisy strain estimates. We use the same parameter choices as in Kreemer et al. (2018), which means that the spatial resolution is ~100 km. For 24 epochs throughout 1 year, we calculate strain (and rotation) at a regular 0.2° grid of evaluation points and fit the displacements with an average root-mean-square of ~0.3 mm per epoch. The vertical seasonal displacements are estimated on a similar grid using the GPS Imaging technique presented by Hammond et al. (2016).

We deliberately choose a low spatial resolution, because our aim is to extract significant strain signals over large areas. An increase in the spatial resolution could be accomplished by considering strain from increasingly smaller station triangles. However, because strain is a spatial derivative, an increase in noise in the displacement data will affect the strain estimates, increasing the uncertainty in the MELD estimate. For example, for our choice of spatial resolution (~100 km) the signal-to-noise ratio (SNR) in strain (measured by its second invariant) is $\geq$2 for 78% of the evaluation points (over all epochs). For ~50-km resolution this is true for 54% of the points and for ~25 km only for 36%.

For the majority of the time and places (but particularly in California), we find that the seasonal strain is dominated by dilatational strain (i.e., $\varepsilon_1 + \varepsilon_2$, where ε_1 and ε_2 are the largest and smallest principal strains, respectfully) rather than shear strain (defined as $\min(|\varepsilon_1|, |\varepsilon_2|)$ whenever the principal strains are of opposite sign). The spatiotemporal variation in shear strain is shown as dynamic content in the supporting information. Figure 2 shows the dilatational strain field at the epochs when it is at an absolute maximum (i.e., 1 April and 1 October). On 1 April strain is contractional through most of California, although it is much larger (i.e., up to -5×10^{-9}) in northern versus southern California. In northern California at that time the SNR is mostly $>$6, and the contractional strain in all of California is oriented orthogonal to the continental margin and the strike of the Sierra Nevada Mountains. In the spring most of the Great Basin is under extension. The signal is

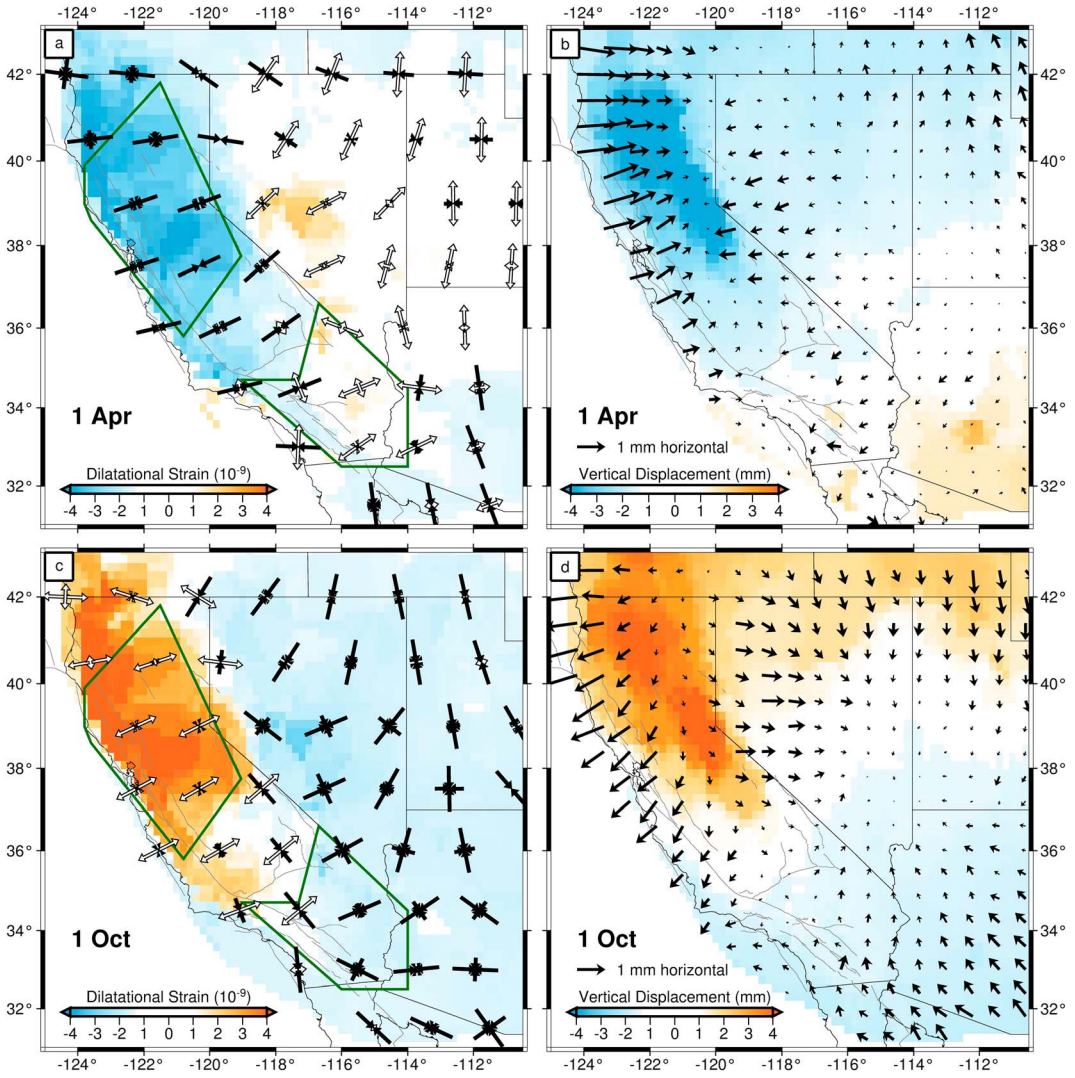

Figure 2. (a) Dilatational strain (positive is extension, negative is contraction) on 1 April. Superimposed are the orientations and relative size of the principal axes: white vectors are positive (extensional) and black are negative (contractional). Principal axes reflect averages for a set of nonoverlapping areas of equal size, and for each set the largest axis is normalized to unity. Gray lines are major faults (i.e., with Quaternary slip rate $\geq$ 2.5 mm/year). (b) Vertical displacements inferred from the GPS Imaging technique (Hammond et al., 2016). Superimposed are horizontal displacements (spatially downsampled) derived from MELD (Kreemer et al., 2018). (c, d) Same as Figures 2a and 2b, respectfully, but instead for 1 October. An animation of a yearly cycle is provided as dynamic content in the supporting information.

reversed in the fall (Figures 2c and 2d). Figure S2 shows the dilatational strain for both epochs for models that consider all data; the main signals are the same.

There is a clear association between the regional horizontal dilatational strain and the vertical displacements, at least in northern California, although there the maximum subsidence is more localized than the contractional area. The causal relationship is best expressed when we superimpose the modeled horizontal displacements onto the vertical field (Figures 2b and 2d); Earth's surface moves toward and away from the northern Sierra Nevada Mountains when those are going down and up in the spring and fall, respectively. An animated image of our results through one entire annual cycle, as well as uncertainties and SNR's (which are mostly $>$1), is provided as dynamic content in the supporting information. All numerical values (data and model) presented in this paper can be found there as well.

We calculate the seasonal variation in the area-weighted average dilatation (i.e., the relative change in area) within a polygon in northern and southern California (Figures 3a and 3b). These polygons (shown in Figure 2)

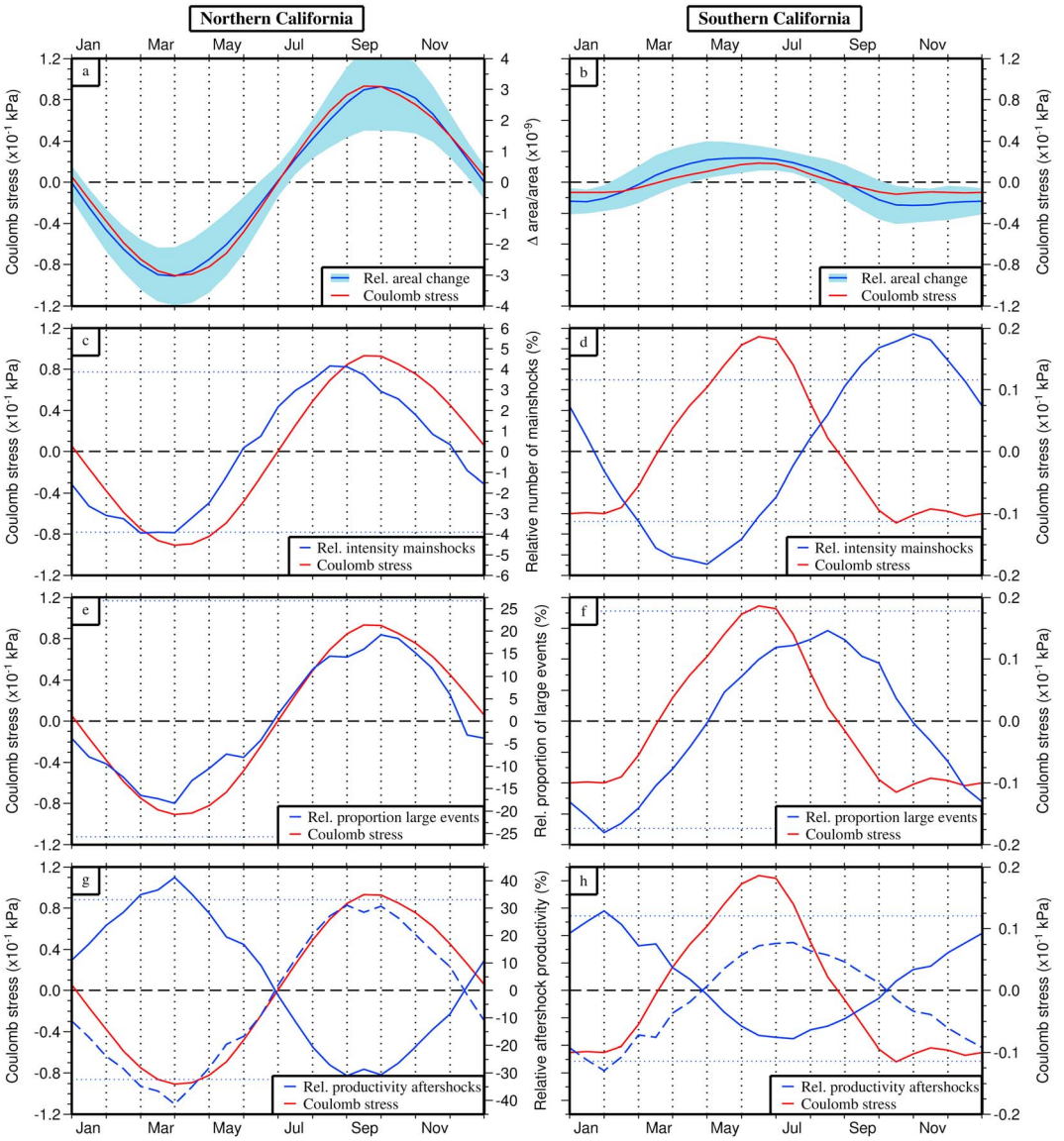

Figure 3. Left and right columns show results for polygons in northern and southern California, respectively. (a, b) Blue line shows seasonal variation in relative areal change (and the standard deviation therein). Red line indicates variation in Coulomb stress on a fault trending 35°W inferred from the strain tensor. Remaining panels (c–h) show in red the same Coulomb stress variations (with the results for southern California scaled up), blue lines show the examined statistic, temporally smoothed, and expressed relative to the median of all epochs (see section 3 and equation (1)) and thin dotted lines indicate the 5% and 95% empirical limits for each examined indicator, inferred by repeating the same analysis on multiple catalogs with reshuffled event times. (c, d) Number of mainshocks with $m \geq 2.5$. (e, f) Proportion of mainshocks with magnitude above or equal to 4.5 among mainshocks with magnitude above or equal to 3.5. (g, h) Aftershock productivity per cluster; see equation (2), and the negative value (dashed line). The axis description between the left and right panels applies to both panels.

are chosen to capture an as spatially-coherent signal as possible while also being constrained by the footprint of the seismicity catalogs with which we compare the results (section 3). The calculation of average dilatation per epoch also uses the variance in the dilatational strain as weight. Figures 3a and 3b also show the weighted one standard deviation in the relative areal strain, which mostly expresses spatial variation. The seasonal variation in strain is significant for both regions, but the signal is out of phase by 4 months between them and the amplitude in relative areal strain is ~3 times as large in the north compared to the south. Figure S3 shows the seasonal variation in relative areal change based on models using all GPS

displacements; the variation is the same and while uncertainties for northern California are slightly larger than those in Figure 3, seasonality is still significant.

Next, we convert the strain into a Coulomb stress on a vertical fault with azimuth of 35°W (i.e., an average for the San Andreas fault [SAF] system) and show the average for each polygon in Figure 3. For this conversion we use the relationships of King et al. (1994), assume a coefficient of friction of 0.4, and use a Young's modulus of 50 GPa to convert strain to stress. The seasonal variation in Coulomb stress very closely follows the same phase and relative amplitudes as the relative areal strain in both polygons. This indicates that for the SAF, which trends orthogonal to the main dilatational strain orientation, the seasonal variations in Coulomb stress are controlled by those in dilatational strain, which are oriented orthogonal to the fault.

3. Seasonal Variations in Seismicity and Correlation With Strain

We explore correlations between seismicity and temporal variations in relative Coulomb stress in northern and southern California by using the relocated catalogs of Waldhauser and Schaff (2008) from 1984 to 2012 and Hauksson et al. (2012) from 1981 to 2014, respectively. For northern California we exclude the induced seismicity near the Geysers, CA. The minimal examined magnitude in both catalogs is 2.0, which is slightly above or equal to the completeness magnitude according to, for example, Wiemer and Wyss (2000) and Johnson et al. (2017b).

We separate mainshocks from aftershocks and foreshocks by identifying earthquake clusters using the nearest-neighbor earthquake distance approach (Zaliapin et al., 2008; Zaliapin & Ben-Zion, 2013, 2016). Every cluster is comprised of a single mainshock and possible foreshocks and aftershocks. We examine two statistics related to mainshocks and one statistic related to aftershocks.

For each earthquake we consider its timing $0 \le t < 1$ within an annual cycle (1 January to 31 December) and work with a stacked data set with event times within the interval [0, 1]. We smooth all earthquake statistics by considering a moving time window of 8 months (or 8/12 in the dimensionless units of the unit time interval) within which we apply a centered Gaussian weighting kernel with standard deviation of 2 months. This substantial temporal smoothing turns out to be instrumental in revealing the correlations that we report and is warranted for two reasons. First, smoothing is justified by the observed and predicted phase shift of up to 3 months between annual stress perturbations and seismic intensity (Ader et al., 2014). Second, the seasonality is hidden in the noise in a conventional stacking analysis. For instance, if we sort the mainshocks in 24 bins (i.e., ~½ month per bin, consistent with the strain analysis) and plot demeaned relative values (Figure S4), seasonality is hard to detect, particularly for northern California. We notice, however, that a sinusoidal fit to the stacked data reveals the correct phase of a seasonal signal. If we introduce some smoothing and produce a time series of the Seasonality Index (SI), seasonality in the data becomes evident. Specifically, we define the SI as $100(N_1 - N_2)/(N_1 + N_2)$, where N_1 is the number of events within the 6-month period centered on the examined epoch and N_2 is the number of events in the preceding 6-month period. This definition is adapted from the one proposed by Walsh and Lawler (1981) based on monthly data. The difference between the stacked data and the SI becomes evident when we fit a sinusoidal function with annual period to each (Figure S4). While the phase of the two models is the same, the relative amplitude is higher for the fit to the SI values and the root-mean-square misfit to the SI values is ~24 and ~14 times lower for northern and southern California, respectively, than the misfit with the stacked data. In conclusion, multiple alternative smoothing techniques reveal smoothly varying numbers of mainshocks from season to season. The analysis shown in the main text produces the most clear, robust, and visually appealing signal.

To ensure uniformity of the reported values, for each examined earthquake statistic S we show its linear transformation S_{median} as follows:

$$S_{\text{median}} = \frac{S - \text{median}(S)}{\text{median}(S)}. \quad (1)$$

Here median (S) is the sample median of the statistic's values.

We first examine the seasonal variation in the annual number of mainshocks with $m \ge 2.5$ (Figures 3c and 3d). The relative amplitude and phase of the variation in mainshocks are very similar to that in the SI inferred from

the stacked data (Figure S4). Both approaches thus show the same seasonal variation, which supports the chosen amount of smoothing. The mainshock intensity values are shown together with the Coulomb stress. In the north (Figure 3c), we observe a strong positive correlation between mainshock intensity (blue) and Coulomb stress (red), with a phase shift of about a month. In the south (Figure 3d), a statistically significant fluctuation of mainshock intensity is not related to the stress changes.

Figures 3e and 3f compare Coulomb stress with the proportion of larger mainshocks, those with $m > 4.5$, among mainshocks with magnitude $m > 3.5$. The proportion of larger mainshocks is a robust and crude (reciprocal) analog to fluctuations in the b value. In the north (Figure 3e), there is an almost perfect match between the examined curves. In the south (Figure 3f), there exists a strong positive correlation, with a phase shift of 2 months.

Figures 3g and 3h show a comparison of Coulomb stress with the aftershock productivity. Specifically, we examine the numbers A_i of aftershocks within ith earthquake cluster. To eliminate the exponential increase of the aftershock number A_i with the magnitude m_i of the cluster mainshock (e.g., Zaliapin & Ben-Zion, 2013), we normalize the aftershock counts:

$$a_i = \frac{A_i}{A(m_i)}, \tag{2}$$

using the average number A (m) of aftershocks within clusters with mainshock magnitude $m \pm \delta$, where $\delta = 0.1$. The final analysis is done using the values of a_i. The normalized aftershock production is negatively correlated with Coulomb stress, in both the north and south.

On every panel in Figure 3 we also show the 5% and 95% empirical limits for each examined indicator, inferred by repeating the same analysis on multiple catalogs with reshuffled event times.

In the aftershock productivity analysis (Figures 3g and 3h), we reshuffled the timing of clusters, keeping the respective aftershock counts assigned to each cluster. The seasonal peaks for most indicators reach or exceed the confidence interval indicated in the figure, except for proportion of large earthquakes in northern California.

For most comparisons between seismicity indicators and Coulomb stress we find a strong (anti)correlation. Notably, these correlations follow the 4-month phase difference between northern and southern California Coulomb stress curves. The only exception is seen for the intensity of mainshocks in southern California (discussed below).

4. Discussion and Conclusions

We find significant, spatially coherent, seasonal variations in the horizontal dilatational strain field. These variations are out of phase between northern and southern California, as well as the Great Basin. The largest peak-to-peak variation occurs in northern California, where the largest vertical displacements occur as well. The vertical seasonal displacement has been shown to largely reflect hydrological loading (Amos et al., 2014; Argus et al., 2014), which has also been shown to explain interannual vertical displacements (Argus et al., 2017; Borsa et al., 2014). Horizontal contraction is predicted underneath a surface load and extension away from the load (Bevis et al., 2016; Wahr et al., 2013), which we observe in northern California and Nevada, respectively, in a direction normal to the load. In addition, loading is expected to cause mostly dilatational surface strain and minimal shear (in a uniform elastic medium), which we observe. We therefore infer that hyrological loading is likely the main driver of the observed horizontal seasonal strain, at least in the northern part of our study area.

The load is spread out beyond the northern Sierra Nevada Mountains and over the entire northern area of the state, as expressed by the wide zone of subsidence and contraction. The fact that maximum subsidence in southern California occurs earlier, and at a lower amplitude, than in northern California, could be ascribed to an absence of a large snow packs and large reservoirs in the south, which would facilitate a quick runoff. As a result, thermoelastic strain may also be more significant than loading-induced strain in the south than in the north (Ben-Zion & Allam, 2013; Prawirodirdjo et al., 2006; Tsai, 2011). In any case, in our study we do not

concern ourselves with the exact mechanisms that cause the strain variations and focus on the correlations with seismicity.

Our modeled strain values are only a few nanostrains. They are so small partly because of our approach to focus on large-scale strain signals that can be robustly resolved. Consequently, our Coulomb stresses are also at least an order of magnitude smaller than those reported by Kraner et al. (2018) for the Napa fault region in northern California. Our Coulomb stress variations are also at least an order of magnitude smaller than those predicted by hydrological loading (Amos et al., 2014; Johnson et al., 2017a, 2017b). Again, this may be a result of our focus on large areas. We find that the small values are not the result of the amount of smoothing we apply. The actual strain, and thus Coulomb stress, for a small area may be much larger, but we find the statistical significance of those strains to be much lower than what we present here. In any case, we are interested in comparing the strain and seismicity within a larger area, and hence we focus on the phase and relative amplitude of the signals.

We find a distinct 4-month phase lag between the maximum area growth or Coulomb stress for the northern and southern California polygons. Most seismicity indicators we consider are within 1-month in-phase or out of phase with the deformation signal and thus generally follow that phase lag between north and south. The only exception is the variation of mainshock intensity in the south (Figure 4b). It does show a significant seasonal signal but one that is out-of-phase with the respective seasonal strain/stress. While it is hard to assess the cause of the seasonality in mainshock intensity there, the fact that it is out-of-phase with the seasonal deformation may be because, compared to the north, the deformation field is less homogeneous, there is more variation between the orientation of deformation and faulting, and the strain/stress amplitudes are lower. In the north, the seasonal strain seems directly linked to fault-normal stress perturbations (i.e., unclamping of the fault) that trigger earthquakes and allow smaller events to grow larger. In the south, other seasonal effects, such as thermoelastic strain, may contribute more significantly than any loading-induced strain to the observed seasonal strain.

While stress perturbations of the kinds we observe may not trigger events in the south, the fact that we do see a correlation in both regions between an increase in Coulomb stress and the proportion of larger events may suggest that when an earthquake happens at times of an increased seasonal Coulomb stress, the favorable stress regime allows for earthquakes to grow larger than they otherwise would. Consequently, the larger events cause more stress release, reducing the need for (more) aftershocks, which explains the observed negative correlation with aftershock productivity.

Our results add nuance to the observations of Christiansen et al. (2005), who found a peak in seismicity intensity in the fall for four out of the five volcanic centers that they examined in the western United States and that had significant seasonal variation in shallow seismicity or to those of Christiansen et al. (2007), who observed more earthquakes in the fall along the central SAF creeping section. Our analysis shows similar variations, but much more unambiguously, and link them to seasonal strain/stress. Moreover, we show that when considering mainshocks and aftershocks separately, one may find different correlations with seasonal deformation for different areas and that the intensity of mainshocks may not always be the proper indicator of seasonality.

Periodic variations in seismic intensity are predicted when stress perturbations of similar period are applied to a fault (Ader et al., 2014; Beeler & Lockner, 2003; Brinkman et al., 2016; Dieterich, 1987). Our results confirm those predictions, and the phase-difference observed here (±1 month) can be compared with those predicted such that the variables and properties used in rate-and-state friction models or laboratory experiments can be reconsidered. In any case, we present evidence how horizontal seasonal strain relates to seismicity variations, and we conclude that the nuance between the behavior of mainshocks and aftershocks may provide insights to further our understanding of seismogenesis.

Acknowledgments
This work would not be possible without the numerous groups operating GPS stations and those that archive the data (see supporting information). We thank W. Hammond for making the GPS Imaging code available and Z. Young for applying it to the vertical displacements. We appreciate comments made by Y. Ben-Zion, Z.-K. Shen, and an anonymous reviewer. All figures were created using Generic Mapping Tools (Wessel & Smith, 1998). This work was funded by NASA award NNX16AK89G to C. K., NSF award EAR1723033 to I. Z., and USGS NEHRP award G18AP00019 to both. This research was supported by the Southern California Earthquake Center (contribution 8125). SCEC is funded by NSF cooperative agreement EAR-1033462 and USGS cooperative agreement G12AC20038.

References

Ader, T. J., & Avouac, J.-P. (2013). Detecting periodicities and declustering in earthquake catalogs using the Schuster spectrum, application to Himalayan seismicity. *Earth and Planetary Science Letters*, *377–378*, 97–105. https://doi.org/10.1016/j.epsl.2013.06.032

Ader, T. J., Lapusta, N., Avouac, J.-P., & Ampuero, J.-P. (2014). Response of rate-and-state seismogenic faults to harmonic shear-stress perturbations. *Geophysical Journal International*, *198*(1), 385–413. https://doi.org/10.1093/gji/ggu144

Amos, C. B., Audet, P., Hammond, W. C., Bürgmann, R., Johanson, I. A., & Blewitt, G. (2014). Uplift and seismicity driven by groundwater depletion in central California. *Nature*, *509*(7501), 483–486. https://doi.org/10.1038/nature13275

Argus, D. F., Fu, Y., & Landerer, F. W. (2014). Seasonal variation in total water storage in California inferred from GPS observations of vertical land motion. *Geophysical Research Letters*, *41*, 1971–1980. https://doi.org/10.1002/2014GL059570

Argus, D. F., Heflin, M. B., Peltzer, G., Crampe, F., & Webb, F. H. (2005). Interseismic strain accumulation and anthropogenic motion in metropolitan Los Angeles. *Journal of Geophysical Research*, *110*, B04401. https://doi.org/10.1029/2003JB002934

Argus, D. F., Landerer, F. W., Wiese, D. N., Martens, H. R., Fu, Y., Famiglietti, J. S., et al. (2017). Sustained water loss in California's mountain ranges during severe drought from 2012 to 2015 inferred from GPS. *Journal of Geophysical Research: Solid Earth*, *122*, 10,559–10,585. https://doi.org/10.1002/2017JB014424

Beeler, N. M., & Lockner, D. A. (2003). Why earthquakes correlate weakly with the solid Earth tides: Effects of periodic stress on the rate and probability of earthquake occurrence. *Journal of Geophysical Research*, *108*(B8), 2391. https://doi.org/10.1029/2001JB001518

Ben-Zion, Y., & Allam, A. A. (2013). Seasonal thermoelastic strain and postseismic effects in Parkfield borehole dilatometers. *Earth and Planetary Science Letters*, *379*, 120–126. https://doi.org/10.1016/j.epsl.2013.08.024

Bettinelli, P., Avouac, J.-P., Flouzat, M., Bollinger, L., Ramillien, G., Rajaure, S., & Sapkota, S. (2008). Seasonal variations of seismicity and geodetic strain in the Himalaya induced by surface hydrology. *Earth and Planetary Science Letters*, *266*(3–4), 332–344. https://doi.org/10.1016/j.epsl.2007.11.021

Bevis, M., Melini, D., & Spada, G. (2016). On computing the geoelastic response to a disk load. *Geophysical Journal International*, *205*(3), 1804–1812. https://doi.org/10.1093/gji/ggw115

Blewitt, G., Hammond, W. C., & Kreemer, C. (2018). Harnessing the GPS data explosion for interdisciplinary science. *EOS*. https://doi.org/10.1029/2018ES005636

Blewitt, G., Kreemer, C., Hammond, W. C., & Goldfarb, J. M. (2013). Terrestrial reference frame NA12 for crustal deformation studies in North America. *Journal of Geodynamics*, *72*, 11–24. https://doi.org/10.1016/j.jog.2013.08.004

Blewitt, G., Lavalée, D., Clarke, P., & Nurutdinov, K. (2001). A new global mode of Earth deformation: Seasonal cycle detected. *Science*, *294*(5550), 2342–2345. https://doi.org/10.1126/science.1065328

Bollinger, L., Perrier, F., Avouac, J.-P., Sapkota, S., Gautam, U., & Tiwari, D. R. (2007). Seasonal modulation of seismicity in the Himalaya of Nepal. *Geophysical Research Letters*, *34*, L08304. https://doi.org/10.1029/2006GL029192

Borsa, A. A., Agnew, D. C., & Cayan, D. R. (2014). Ongoing drought-induced uplift in the western United States. *Science*, *345*(6204), 1587–1590. https://doi.org/10.1126/science.1260279

Braunmiller, J., Nábělek, J. L., & Tréhu, A. M. (2014). A seasonally modulated earthquake swarm near Maupin, Oregon. *Geophysical Journal International*, *197*(3), 1736–1743. https://doi.org/10.1093/gji/ggu081

Brinkman, B. A. W., LeBlanc, M. P., Uhl, J. T., Ben-Zion, Y., & Dahmen, K. A. (2016). Probabilistic model of waiting times between large failures in sheared media. *Physical Review E*, *93*(1), 013003. https://doi.org/10.1103/PhysRevE.93.013003

Chanard, K., Avouac, J. P., Ramillien, G., & Genrich, J. (2014). Modeling deformation induced by seasonal variations of continental water in the Himalaya region: Sensitivity to Earth elastic structure. *Journal of Geophysical Research: Solid Earth*, *119*, 5097–5113. https://doi.org/10.1002/2013JB010451

Christiansen, L., Hurwitz, S., & Ingebritsen, S. E. (2007). Annual modulation of seismicity along the San Andreas Fault near Parkfield, CA. *Geophysical Research Letters*, *34*, L04306. https://doi.org/10.1029/2006GL028634

Christiansen, L. B., Hurwitz, S., Saar, M. O., Ingebritsen, S. E., & Hsieh, P. A. (2005). Seasonal seismicity at western United States volcanic centers. *Earth and Planetary Science Letters*, *240*(2), 307–321. https://doi.org/10.1016/j.epsl.2005.09.012

Craig, T. J., Chanard, K., & Calais, E. (2017). Hydrologically-driven crustal stresses and seismicity in the New Madrid seismic zone. *Nature Communications*, *8*(1), 2143. https://doi.org/10.1038/s41467-017-01696-w

Dieterich, J. H. (1987). Nucleation and triggering of earthquake slip: Effect of periodic stresses. *Tectonophysics*, *144*(1-3), 127–139. https://doi.org/10.1016/0040-1951(87)90012-6

Drouin, V., Heki, K., Sigmundsson, F., Hreinsdóttir, S., & Ófeigsson, B. G. (2016). Constraints on seasonal load variations and regional rigidity from continuous GPS measurements in Iceland, 1997–2014. *Geophysical Journal International*, *205*(3), 1843–1858. https://doi.org/10.1093/gji/ggw122

Dutilleul, P., Johnson, C. W., Bürgmann, R., Wan, Y., & Shen, Z.-K. (2015). Multifrequential periodogram analysis of earthquake occurrence: An alternative approach to the Schuster spectrum, with two examples in central California. *Journal of Geophysical Research: Solid Earth*, *120*, 8494–8515. https://doi.org/10.1002/2015JB012467

Elósegui, P., Davis, J. L., Mitrovica, J. X., Bennett, R. A., & Wernicke, B. P. (2003). Crustal loading near Great Salt Lake, Utah. *Geophysical Research Letters*, *30*(3), 1111. https://doi.org/10.1029/2002GL016579

Fu, Y., Argus, D. F., Freymueller, J. T., & Heflin, M. B. (2013). Horizontal motion in elastic response to seasonal loading of rain water in the Amazon Basin and monsoon water in Southeast Asia observed by GPS and inferred from GRACE. *Geophysical Research Letters*, *40*, 6048–6053. https://doi.org/10.1002/2013GL058093

Gao, S. S., Silver, P. G., Linde, A. T., & Sacks, I. S. (2000). Annual modulation of triggered seismicity following the 1992 Landers earthquake in California. *Nature*, *406*(6795), 500–504. https://doi.org/10.1038/35020045

Grapenthin, R., Sigmundsson, F., Geirsson, H., Árnadóttir, T., & Pinel, V. (2006). Icelandic rhythmics: Annual modulation of land elevation and plate spreading by snow load. *Geophysical Research Letters*, *33*, L24305. https://doi.org/10.1029/2006GL028081

Hammond, W. C., Blewitt, G., & Kreemer, C. (2016). GPS imaging of vertical land motion in California and Nevada: Implications for Sierra Nevada uplift. *Journal of Geophysical Research: Solid Earth*, *121*, 7681–7703. https://doi.org/10.1002/2016JB013458

Hauksson, E., Yang, W., & Shearer, P. M. (2012). Waveform relocated earthquake catalog for Southern California (1981 to June 2011). *Bulletin of the Seismological Society of America*, *102*(5), 2239–2244. https://doi.org/10.1785/0120120010

Heki, K. (2001). Seasonal modulation of interseismic strain buildup in northeastern Japan driven by snow loads. *Science*, *293*(5527), 89–92. https://doi.org/10.1126/science.1061056

Heki, K. (2003). Snow load and seasonal variation of earthquake occurrence in Japan. *Earth and Planetary Science Letters*, *207*(1–4), 159–164. https://doi.org/10.1016/S0012-821X(02)01148-2

Johnson, C. W., Fu, Y., & Bürgmann, R. (2017a). Seasonal water storage, stress modulation, and California seismicity. *Science*, *356*(6343), 1161–1164. https://doi.org/10.1126/science.aak9547

Johnson, C. W., Fu, Y., & Bürgmann, R. (2017b). Stress models of the annual hydrospheric, atmospheric, thermal, and tidal loading cycles on California faults: Perturbation of background stress and changes in seismicity. *Journal of Geophysical Research: Solid Earth*, *122*, 10,605–10,625. https://doi.org/10.1002/2017JB014778

King, G. C. P., Stein, R. S., & Lin, J. (1994). Static stress changes and the triggering of earthquakes. *Bulletin of the Seismological Society of America*, *84*(3), 935–953.

Kraner, M. L., Holt, W. E., & Borsa, A. A. (2018). Seasonal non-tectonic loading inferred from cGPS as a potential trigger for the M6.0 South Napa Earthquake. *Journal of Geophysical Research: Solid Earth*, *123*, 5300–5322. https://doi.org/10.1029/2017JB015420

Kreemer, C., Hammond, W. C., & Blewitt, G. (2018). A robust estimation of the 3-D intraplate deformation of the North American plate from GPS. *Journal of Geophysical Research-Solid Earth*, *123*, 4388–4412. https://doi.org/10.1029/2017JB015257

Matsumura, K. (1986). On regional characteristics of seasonal variation of shallow earthquake activities in the world. *Bulletin of the Disaster Prevention Research Institute*, *36*(2), 43–98.

Panza, G. F., Peresan, A., & Zuccolo, E. (2011). Climatic modulation of seismicity in the Alpine–Himalayan mountain ranges. *Terra Nova*, *23*(1), 19–25. https://doi.org/10.1111/j.1365-3121.2010.00976.x

Pollitz, F., Wech, A., Kao, H., & Bürgmann, R. (2013). Annual modulation of non-volcanic tremor in northern Cascadia. *Journal of Geophysical Research: Solid Earth*, *118*, 2445–2459. https://doi.org/10.1002/jgrb.50181

Prawirodirdjo, L., Ben-Zion, Y., & Bock, Y. (2006). Observation and modeling of thermoelastic strain in Southern California Integrated GPS Network daily position time series. *Journal of Geophysical Research: Solid Earth*, *111*, B02408. https://doi.org/10.1029/2005JB003716

Tsai, V. C. (2011). A model for seasonal changes in GPS positions and seismic wave speeds due to thermoelastic and hydrologic variations. *Journal of Geophysical Research: Solid Earth*, *116*, B04404. https://doi.org/10.1029/2010JB008156

van Dam, T. M., Blewitt, G., & Heflin, M. B. (1994). Atmospheric pressure loading effects on Global Positioning System coordinate determinations. *Journal of Geophysical Research*, *99*(B12), 23,939–23,950. https://doi.org/10.1029/94JB02122

van Dam, T. M., Wahr, J., Milly, P. C. D., Shmakin, A. B., Blewitt, G., Lavallée, D., & Larson, K. M. (2001). Crustal displacements due to continental water loading. *Geophysical Research Letters*, *28*(4), 651–654. https://doi.org/10.1029/2000GL012120

Wahr, J., Khan, S. A., van Dam, T., Liu, L., van Angelen, J. H., van den Broeke, M. R., & Meertens, C. M. (2013). The use of GPS horizontals for loading studies, with applications to northern California and southeast Greenland. *Journal of Geophysical Research: Solid Earth*, *118*, 1795–1806. https://doi.org/10.1002/jgrb.50104

Waldhauser, F., & Schaff, D. P. (2008). Large-scale relocation of two decades of Northern California seismicity using cross-correlation and double-difference methods. *Journal of Geophysical Research*, *113*, B08311. https://doi.org/10.1029/2007JB005479

Walsh, R. P. D., & Lawler, D. M. (1981). Rainfall seasonality: Description, spatial patterns and change through time. *Weather*, *36*(7), 201–208. https://doi.org/10.1002/j.1477-8696.1981.tb05400.x

Wessel, P., & Smith, W. H. F. (1998). New, improved version of the Generic Mapping Tools released. In *EOS. Trans. AGU*, *79*(47), 579. https://doi.org/10.1029/98EO00426

Wiemer, S., & Wyss, M. (2000). Minimum magnitude of completeness in earthquake catalogs: Examples from Alaska, the Western United States, and Japan. *Bulletin of the Seismological Society of America*, *90*(4), 859–869. https://doi.org/10.1785/0119990114

Wu, X., Heflin, M. B., Ivins, E. R., Argus, D. F., & Webb, F. H. (2003). Large-scale global surface mass variations inferred from GPS measurements of load-induced deformation. *Geophysical Research Letters*, *30*(14), 1742. https://doi.org/10.1029/2003GL017546

Zaliapin, I., & Ben-Zion, Y. (2013). Earthquake clusters in southern California I: Identification and stability. *Journal of Geophysical Research: Solid Earth*, *118*, 2847–2864. https://doi.org/10.1002/jgrb.50179

Zaliapin, I., & Ben-Zion, Y. (2016). A global classification and characterization of earthquake clusters. *Geophysical Journal International*, *207*(1), 608–634. https://doi.org/10.1093/gji/ggw300

Zaliapin, I., Gabrielov, A., Keilis-Borok, V., & Wong, H. (2008). Clustering analysis of seismicity and aftershock identification. *Physical Review Letters*, *101*(1), 018501. https://doi.org/10.1103/PhysRevLett.101.018501